Dynamic Modeling and Control of Self-Oscillating Parallel Resonant Converters Based on a Variable Structure Systems Approach

Ricardo Bonache-Samaniego, Carlos Olalla, *Member, IEEE*, and Luis Martínez-Salamero, *Senior Member, IEEE*

***Abstract*—This paper describes a novel modeling approach for self-oscillating resonant power converters operating under a control method based on the variable structure of the system (VSS). Using a fundamental harmonic approximation, the link between control and switching frequency in steady state is found to be accurately described by an affine function that depends on the load. Besides, this link has been extended in order to characterize the control-to-switching frequency dynamics, resulting in a novel small-signal continuous-time model. The resulting control-to-switching frequency transfer function can be appended to the well-known models for frequency modulation, in order to obtain a complete control-to-output system. The new model exposes that the dynamics of the converter under the VSS-based control approach presents advantages with respect to the conventional methods as frequency modulation: 1) reduced dc gain variation for uncertain loads and 2) improved phase margin at high frequencies. The dynamic modeling is complemented with the design of a controller for regulating the output voltage of a parallel resonant converter, whose performance and robustness are compared with the standard frequency modulation. Numerical simulations and experimental results confirm and verify the analytical derivations.**

***Index Terms*—Modeling of power converters, parallel resonant converter, resonant power conversion, robust control, self-oscillating control, series resonant converter, variable structure system.**

I. Introduction

RESONANT conversion plays a key role in today's power processing systems. First, resonant converters can provide, among other advantages, reduced switching loss and improved power density, with respect to their pulsewidth-modulated counterparts. Besides, resonant conversion is inherently related to a number of applications as, for example, efficient lighting [1]–[3] and induction heating [4], [5], to name a few. Typically, these circuits can be controlled by means of frequency, amplitude, or phase modulation [6]–[8]. Due to the large-signal excursion involved in the state variables of the resonant tank, the modeling of resonant converters under such control methods can be considered a complex task. A well-known simplification is based on the approximation of the resonant tank waveforms by their fundamental components. In [9], an intuitive derivation of the transfer functions was proposed, while a more general small-signal model based on time-varying phasors was described in [10]. This last method has been successfully employed for the simulation [11] and modeling [6], [7] of a variety of resonant converters, and it may be considered the standard approach.

In addition to these approximated frequency-domain methods, also the exact response of the resonant tank has been explored. State-plane methods, which can be used for analyzing the soft-switching properties of the converter [12], were first proposed for control in [13], where linear and nonlinear combinations of the states were used to activate the switches, and no voltage-controlled oscillator was required. This idea is the basis for the self-oscillating resonant converters that have appeared since then [14]–[20]. Despite most of these references did not emphasize this, they proposed different forms of controllers based on the variable structure of the system (VSS) [21]. The main advantages of this control approach are: 1) improved regulation performance, 2) reduced-order dynamics, and 3) a straightforward realization. However, for the same reasons stated previously, the modeling of the closed-loop dynamics under VSS-based control is not obvious. The exact trajectories of the series and parallel resonant converters were investigated in [14]–[16], and [22], while the fundamental approximation was employed in [17] and [18]. More recent works have proposed linear piecewise-affine models [19], which allow to demonstrate the closed-loop stability by numerically derived Lyapunov functions [20]. In a previous work [22], it was shown analytically that a limit cycle with an oscillating frequency equal to the resonant frequency could be generated in the PRC using a mechanism for changing input voltage polarity based on the inductor sign. A minimum value of Q to guarantee the oscillations was also established. However, no dynamic modeling neither amplitude regulation of the output voltage were considered. Therefore, in spite of the advantages of this control method, a frequency-domain model has not been reported in the previous literature. This does not allow to assess the dynamic performances of the converter nor to precisely synthesize the parameters of a controller for closed-loop regulation.

In this paper, a novel frequency-domain model is obtained for resonant converters operating under the VSS approach. While

Manuscript received September 7, 2015; revised January 26, 2016; accepted March 2, 2016. Date of publication March 11, 2016; date of current version November 11, 2016. This work was supported in part by the People Programme (Marie Curie Actions) of the European Union's Seventh Framework Programme (FP7/2007-2013) under REA Grant 626117 and in part by the Spanish Ministry of Economy and Competitiveness under Grants DPI2012-31580/BES-2013-063288 and CSD2009-00046. Recommended for publication by Associate Editor M. Ordonez.

The authors are with the Department of Electrical, Electronic, and Automatic Control Engineering, Rovira i Virgili University, Tarragona 43007, Spain (e-mail: ricardo.bonache@urv.cat; carlos.olalla@urv.cat; luis.martinez@urv.cat).

Color versions of one or more of the figures in this paper are available online at http://ieeexplore.ieee.org.

Digital Object Identifier 10.1109/TPEL.2016.2541170

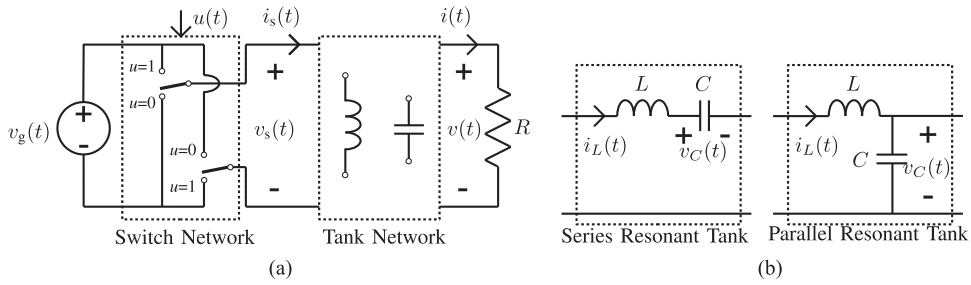

Fig. 1. Circuit diagram of a resonant power converter. (a) Simplified functional schematic. (b) Resonant tanks of the series and parallel resonant converters.

the proposed control law is not new, the paper discusses a modeling approach that allows to link the properties of VSS-based control with the conventional frequency-domain methods. This novel model allows, for first time, to carry out high-performance regulation by employing the parameters of the VSS-based law as control inputs. Besides, this paper demonstrates that this control approach allows to reduce the control-to-output dc gain variation for uncertain loads, and that it yields simpler dynamics up to high frequencies. The accuracy of the proposed model has been illustrated in the case of designing a controller for regulating the output voltage in a parallel resonant converter. The resulting dynamic properties have been compared with a converter controlled by the conventional frequency modulation, proving the advantages that this approach can provide.

This paper is organized as follows. Section II introduces the VSS-based control method and links two possible control laws with the steady-state switching frequency of the converter. This connection is extended in Section III, where the frequency-domain control-to-switching frequency model is presented. In Section IV, a design example illustrates the advantages of this approach, which are compared with the conventional frequency modulation by means of numerical simulations of the closed-loop systems. Experimental results validating both the frequency-domain model and the closed-loop performances are shown in Section V for a 100-W PRC prototype. Section VI summarizes the key aspects of this study and presents some conclusions.

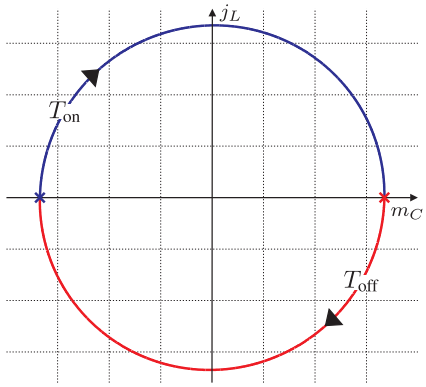

Fig. 2. State-plane normalized trajectory of a PRC controlled by (1): $u = \text{sign}(j_L)$. x marks: switching instants.

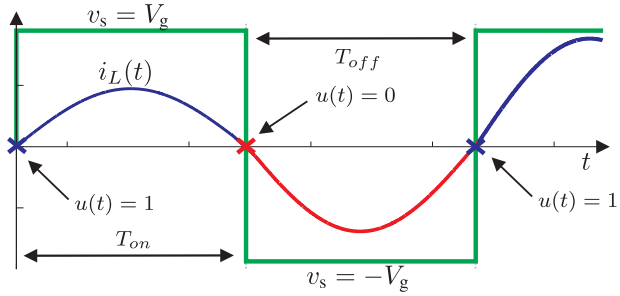

Fig. 3. Waveforms of the PRC controlled by (1): $u = \text{sign}(j_L)$.

II. State-Plane VSS-based Control of Resonant Converters

Fig. 1(a) shows the structure of a full-bridge resonant converter with a generic resonant tank and the load being modeled as a resistance. Assuming a constant input voltage $v_g(t) = V_g$, the switch network produces a square wave of frequency $\omega_{\text{sw}} = \frac{2\pi}{T_{\text{sw}}}$ and subintervals T_{on} $(u = 1)$ and T_{off} $(u = 0)$ at the input of the resonant tank. In this case, the state trajectories of a second-order resonant tank [see Fig. 1(b)] can be easily represented in the plane. Fig. 2 shows the trajectories of a parallel resonant converter near the natural oscillation frequency $\omega_o = \frac{1}{\sqrt{LC}}$ with a sufficiently large quality factor Q. The inductor current and capacitor voltage have been scaled to their normalized values $m_C(t) = \frac{v_C(t)}{V_g}$ and $j_L(t) = \frac{i_L(t)}{V_g/R_o}$, being $R_o = \sqrt{\frac{L}{C}}$ and $Q = \frac{R}{R_o}$. In the figure, the following VSS-based control law activates the switches of the network

$$\begin{cases} \text{If } j_L \geq 0, & \text{activate network topology } T_{\text{on}}(u = 1) \\ \text{If } j_L < 0, & \text{activate network topology } T_{\text{off}}(u = 0) \end{cases} \quad (1)$$

which can also be expressed as a modified sign function $u = \text{sign}(j_L)$.

Given that the switching instants occur at the change of sign in j_L, there is only one possible switching frequency in the limit cycle, where the fundamental harmonic of v_s, denoted v_{s1}, is in phase with the input current, as shown in Fig. 3. The Bode plot of the input impedance $Z_i(s)$, which is depicted in Fig. 4, shows that the phase between the input voltage and the input current is zero at frequency ω_o. Hence, the VSS-based controller in (1) results in the converter switching at the natural oscillation frequency. This observation was already reported in

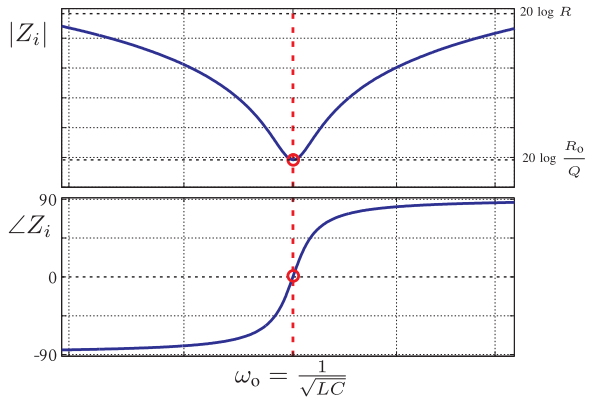

Fig. 4. Bode diagram of $Z_i(s) = \frac{v_{s1}(s)}{j_L(s)}$ for the PRC near the resonant frequency.

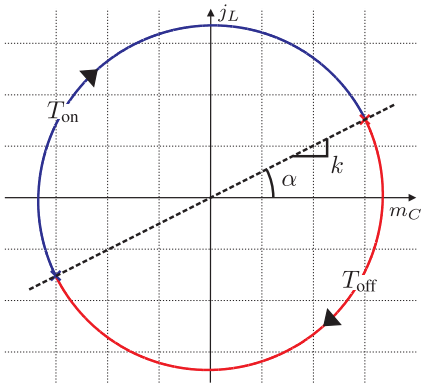

Fig. 5. State-plane normalized trajectory of a PRC controlled by (2): $u = \text{sign}(j_L - km_C)$. x marks: switching instants.

[18] and [22], but employing different descriptions of the trajectories. Since the waveforms are assumed to be approximately sinusoidal, the phase relationship between the input voltage and the input current can be extended to predict the effects of more complex self-oscillating control laws involving a combination of the state variables.

A. Control Principle and Steady-State Model

In general, a linear combination of the states j_L and m_C can be employed to generate the switching instants of the resonant converter. In [14], the switching instants occur when $|s_1 j_L + s_2 m_C| = V_{\text{const}}$ holds, being s_1, s_2, and V_{const} constants. Equivalently, this class of VSS-based controller can also be expressed as

$$u = \text{sign}(j_L - k \cdot m_C). \tag{2}$$

This form, which appeared previously in [16], [19], and[20], has the advantage that it has a straightforward representation in the state plane and, more importantly, that the value of parameter k is directly related to the angle between $v_{s1}(t)$ and $j_L(t)$. Figs. 5 and 6 show the state plane trajectories and the time-domain waveforms of a PRC, now switched following (2). It can be seen that the angle between $v_{s1}(t)$ and $j_L(t)$ is equal to α and

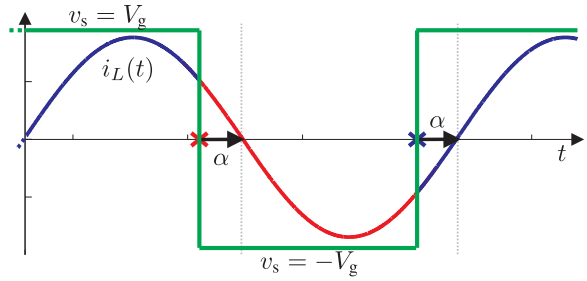

Fig. 6. Waveforms of the PRC controlled by (2): $u = \text{sign}(j_L - km_C)$.

that the slope of the switching boundary is $k = \tan(\alpha)$. Hence, following Fig. 4, when $k > 0$ (positive α), the converter operates above the resonant frequency and when $k < 0$ (negative α) it operates below resonance. An analytic expression of α, given by the input impedance, can be derived as follows:

$$\begin{aligned}
\alpha &= \angle Z_i(s)|_{s=j\omega_{\text{sw}}} \\
&= \angle\left(-\frac{\left(j\frac{\omega_{\text{sw}}}{\omega_o}\right)^2 + j\frac{\omega_{\text{sw}}}{Q\omega_o} + 1}{jC\omega_{\text{sw}} + \frac{1}{R}}\right) \\
&= \angle\left(-\frac{\left(j\frac{\omega_{\text{sw}}}{\omega_o}\right)^2 + j\frac{\omega_{\text{sw}}}{Q\omega_o} + 1}{jC\omega_{\text{sw}} + \frac{1}{R}}\right)\left(\frac{\frac{1}{R} - jC\omega_{\text{sw}}}{\frac{1}{R} - jC\omega_{\text{sw}}}\right) \\
&= \angle\left(\left(\frac{\omega_o}{Q} - j\omega_{\text{sw}}\right)\left(-\left(j\frac{\omega_{\text{sw}}}{Q\omega_o} + \left(1 - \left(\frac{\omega_{\text{sw}}}{\omega_o}\right)^2\right)\right)\right)\right) \\
&= \arctan\left(-Q\frac{\omega_{\text{sw}}}{\omega_o}\left(1 - \frac{1}{Q^2} - \left(\frac{\omega_{\text{sw}}}{\omega_o}\right)^2\right)\right).
\end{aligned} \tag{3}$$

This result allows to eliminate the tangent function in k, and to obtain an explicit relationship between the switching frequency ω_{sw} and k.

$$k = \tan(\alpha) = -Q\frac{\omega_{\text{sw}}}{\omega_o}\left(1 - \frac{1}{Q^2} - \left(\frac{\omega_{\text{sw}}}{\omega_o}\right)^2\right). \tag{4}$$

Besides, assuming that the converter operates near the resonant frequency, the previous expression can be linearized around that point, where $\omega_{\text{sw}} = \omega_o + \hat{\omega}_{\text{sw}}$

$$\begin{aligned}
k(\omega_o + \hat{\omega}_{\text{sw}}) &= \frac{(\omega_o + \hat{\omega}_{\text{sw}})\left(1 - \frac{1}{Q^2} - \frac{{\omega_o}^2}{{\omega_o}^2} - \frac{2\omega_o\hat{\omega}_{\text{sw}}}{{\omega_o}^2} - \frac{\hat{\omega}_{\text{sw}}^2}{{\omega_o}^2}\right)}{\frac{-\omega_o}{Q}} \\
&= \frac{1}{Q} + \left(\frac{2Q}{\omega_o}\hat{\omega}_{\text{sw}} + \hat{\omega}_{\text{sw}}\frac{1}{\omega_o Q}\right)\ldots \\
&\quad + \left(\frac{Q}{{\omega_o}^2}\hat{\omega}_{\text{sw}}^2 + \frac{2Q}{{\omega_o}^2}\hat{\omega}_{\text{sw}}^2 + \frac{Q}{{\omega_o}^3}\hat{\omega}_{\text{sw}}^3\right) \\
&\simeq \frac{1}{Q} + \hat{\omega}_{\text{sw}}\left(\frac{2Q}{\omega_o} + \frac{1}{\omega_o Q}\right).
\end{aligned} \tag{5}$$

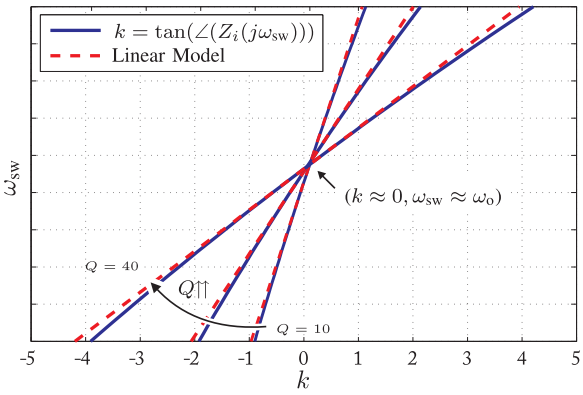

Fig. 7. Exact switching frequency of the PRC with respect to parameter k for three different values of Q = [10, 20, 40] and its linear approximation.

Considering that $2Q \gg 1/Q$, this equation can be rewritten as

$$k = \frac{1}{Q} + 2Q\left(\frac{\omega_{sw}}{\omega_o} - 1\right). \tag{6}$$

Fig. 7 shows the exact nonlinear function (4) and its approximated linear expression (6) for a range of values of k, corresponding to α angles between $[-75, 75]$ degrees. The linear approximation is in good agreement with the nonlinear original expression and provides a direct way to relate the value of k and the switching frequency of the converter. Because this is a direct consequence of the linear phase shape around ω_o, the valid frequency range of this expression shrinks with larger values of Q. In the example of Fig. 7, where values of Q up to 40 are shown, the model can be considered valid for $\alpha \in [-75, 75]$ degrees, providing a wide valid frequency span around resonance.

If k is considered constant, this linear model can be used to obtain the steady-state characteristics of the converter by the conventional frequency-domain methods. As an example, the amplitude of the output voltage in the PRC is

$$V_C = \left|H(s)|_{s=j\left(\left(k-\frac{1}{Q}\right)\frac{\omega_o}{2Q}+\omega_o\right)}\right| V_{s1} \tag{7}$$

where $H(s) = \frac{v_C(s)}{v_{s1}(s)}$ is the voltage transfer function of the tank.

B. Extension to the SRC

Following the same procedure, an analytic expression of α can be derived for the series resonant converter using $\angle Z_i(s)|_{s=j\omega_{sw}}$ and noting that $Q = \frac{R_o}{R}$. The resulting nonlinear expression is

$$k = \tan(\alpha) = Q\left(\frac{\omega_{sw}}{\omega_o} - \frac{\omega_o}{\omega_{sw}}\right) \tag{8}$$

whose linear approximation is similar to the one found for the PRC

$$k = 2Q\left(\frac{\omega_{sw}}{\omega_o} - 1\right) \tag{9}$$

and whose small-signal model relating variations of k and ω_{sw} is the same.

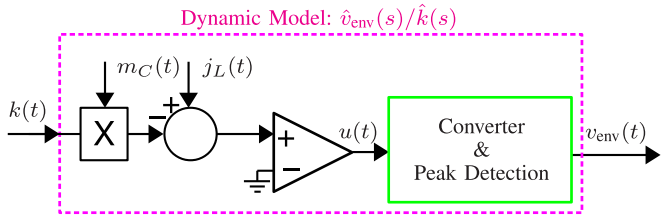

Fig. 8. Block diagram of the converter with the proposed VSS-based controller. The dashed-line box corresponds to the system that is being modeled.

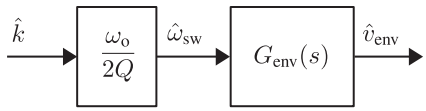

Fig. 9. Block diagram of the small-signal model considering the dc gain $\hat{\omega}_{sw} = \frac{\omega_o}{2Q}\hat{k}$.

III. Dynamic Modeling

This section presents a small-signal modeling approach for resonant converters under the VSS-based control method shown in (2).

The model takes into account the effects of a time varying k in ω_{sw}, such that the resulting transfer function can be appended to the well-known frequency modulated models in, for example, [7]. The results are illustrated with the control-to-output voltage envelope transfer function of a parallel resonant converter as shown in Fig. 8.

First, a dc model that follows from the results of the previous section is introduced. Then, the dynamic effects of a time-varying k are described and modeled in Section III-B.

A. Small-Signal DC Gain

Fig. 9 shows a model for the resonant converter with VSS-based control. The variables are expressed in incremental form, i.e.,: $k(t) = K + \hat{k}(t)$, $\alpha(t) = A + \hat{\alpha}(t)$, and $\omega_{sw}(t) = \Omega_{sw} + \hat{\omega}_{sw}(t)$, with $v_{env}(t) = V_{env} + \hat{v}_{env}(t)$ being the output voltage envelope and $G_{env}(s)$ being the frequency to output voltage envelope transfer function, as in [7]. Note that the time dependence of the incremental variables may be omitted for convenience.

Following the results in (6) and (9), it can be seen that a simple gain connects $\hat{k}$ and $\hat{\omega}_{sw}$

$$\hat{\omega}_{sw} = \frac{\omega_o}{2Q}\hat{k}. \tag{10}$$

The resulting model has appropriate dc gain but there are dynamics that must be considered. The effects of $\hat{k}$ in $\hat{\omega}_{sw}$ are not static, and these are treated in the next subsection. However, this result allows to emphasize the uncertainty reduction effects of the VSS-based controller, due to the dependence of $\hat{\omega}_{sw}$ on Q in (10). Fig. 10(a) depicts the Bode plots of the control-to-output transfer function of a parallel resonant converter with the parameters of Table I. The responses of the converter with the conventional and VSS-based control are shown in dashed and

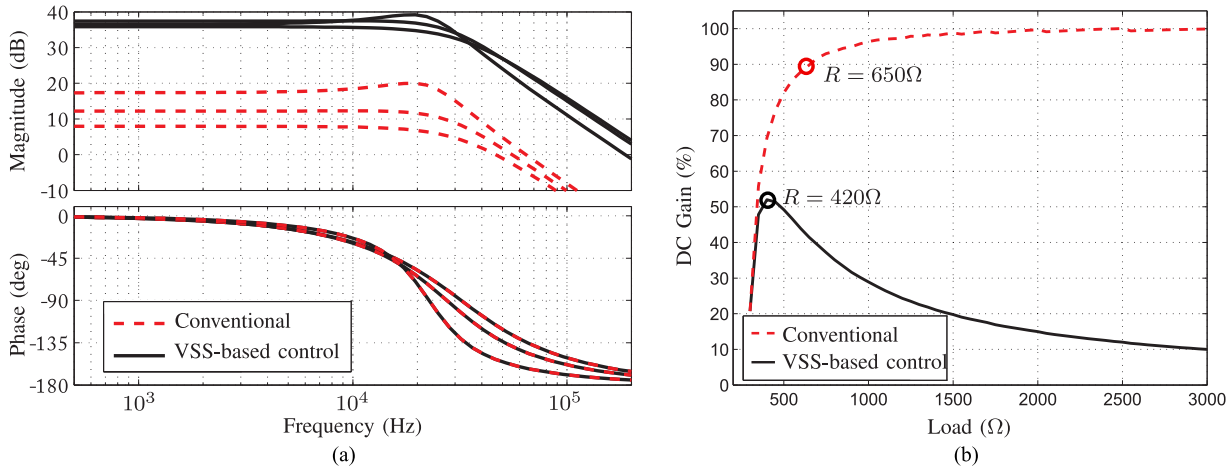

Fig. 10. Effects of VSS-based control on dc gain. (a) Bode plots of $G_{\text{env}}(s)$ and $\frac{\omega_o}{2Q}G_{\text{env}}(s)$ for a set of quality factors $Q = 11, 15, 30$. (b) DC gain against load *R*, considering appropriate switching frequency changes for constant input/output gain.

TABLE I
PARALLEL RESONANT CONVERTER EXAMPLE DESIGN

Parameter	Value
V_{g}	12 V
V_{env}	160 V
L	8.3 μH
C	10.5 nF
$f_{\text{o}} = \frac{\omega_o}{2\pi}$	540 kHz
Q	15

solid lines, respectively. Three different loads, or in other words, three different quality factors $Q = 11, 15, 30$ are shown at the same switching frequency. While the conventionally controlled converter presents a dc gain variation of approximately 10 dB, VSS-based control reduces this uncertainty to negligible values. This reduced dc gain variation can also be observed in Fig. 10(b), where changes in the switching frequency are considered in order to compensate for changes in the load, thus maintaining the same output voltage amplitude. Although the load range has been magnified, it can be seen that, for this set of parameters, VSS-based control reduces the uncertainty of the dc gain by a factor of approximately 1/2. Note that, in such case, the dc gain drops for resistances above 420 Ω because of the inclusion of the term $\frac{\omega_o}{2Q}$, which decreases with increasing loads.

B. Small-Signal Frequency Response for Time-Varying k

The proposed VSS-based controller presents two main dynamic features. First, after a change in $\hat{k}(t)$, there exist a shift of the switching frequency during the next half period. In addition, the settling time of $\hat{\omega}_{\text{sw}}(t)$ is determined by the time constant of the state variables and the quiescent operating point K. While the first effect impacts on the high frequency dynamics, the latter is related to the low frequency response. Assuming linearity, we can formulate the output of the VSS-based controller as a combination of different transfer functions being modeled separately, which are added to obtain the complete model.

1) Switching Frequency Shift: The shift of switching frequency is illustrated in Fig. 11(a). For simplicity, a constant sampling frequency $T = 2/T_{\text{sw}}$ is assumed. The value of $\hat{k}$ is modified between the sampling instants $n-1$ and n, $\Delta\hat{k} = \hat{k}(n) - \hat{k}(n-1)$. This produces a reduced T_{off} time in the half period immediately after. As a consequence, the switching frequency $\hat{\omega}_{\text{sw}_1}(n)$ is increased a factor $\Delta\omega_{_1}$, as shown in Fig. 11(b).

If $\Delta\hat{k}$ is sufficiently small, $\Delta\omega_{_1}$ can be approximated by a proportional relationship between the switching frequency in steady state, when it describes an angle approximately equal to π, and the switching frequency during the first half period, when it describes an angle equal to $\pi - \Delta\hat{\alpha}$

$$\Delta\omega_{_1} = \frac{\Omega_{\text{sw}}}{\pi}\Delta\hat{\alpha} \tag{11}$$

where the angle $\Delta\hat{\alpha}$ can be approximated by

$$\Delta\hat{\alpha} = \arctan(K + \Delta\hat{k}) - \arctan(K) \approx \frac{\Delta\hat{k}}{K^2+1}. \tag{12}$$

Using (11) and (12), a discrete-time model can be posed as follows:

$$\hat{\omega}_{\text{sw}_1}(n) = \frac{\Omega_{\text{sw}}}{\pi}\frac{1}{K^2+1}\left(\hat{k}(n) - \hat{k}(n-1)\right) \tag{13}$$

or equivalently

$$\frac{\hat{\omega}_{\text{sw}_1}(z)}{\hat{k}(z)} = \frac{\Omega_{\text{sw}}}{\pi}\frac{1}{K^2+1}(1 - z^{-1}). \tag{14}$$

This model can be appended to a sampler and a zero-order holder, in order to account for the inherent sampling, and transformed into a continuous-time transfer function using a first-order Pade approximation of the terms $z^{-1} = e^{-\text{s}T}$. The transfer function that models the switching frequency shift can then be

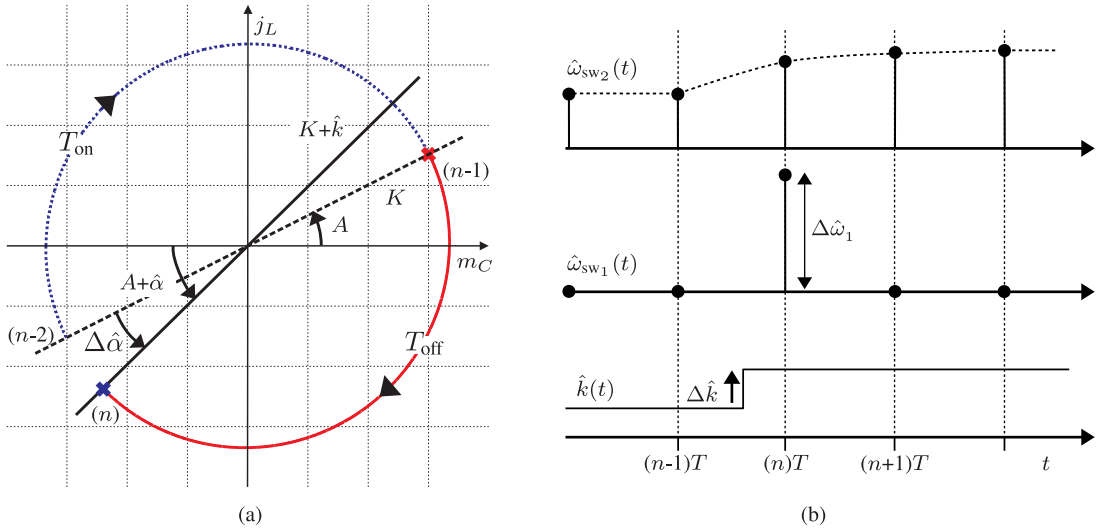

Fig. 11. Changes in the switching frequency due to a time-varying $k(t) = K + \hat{k}(t)$. (a) State-plane normalized trajectory of a PRC controlled by (2) after a change in $\hat{k}$ between instants $(n-1)$ and n. (b) Time-domain waveforms showing the switching frequency shift in $\hat{\omega}_{sw_1}(t)$ and the low frequency response in $\hat{\omega}_{sw_2}(t)$.

written as

$$\frac{\hat{\omega}_{sw_1}(s)}{\hat{k}(s)} = \frac{\Omega_{sw}}{\pi}\frac{1}{K^2+1}\frac{sT}{\left(1+s\frac{T}{2}\right)^2}. \tag{15}$$

Note that, at the sampling instant $(n+1)$, the switching frequency has been assumed to return to its original value, instead of settling down at the expected value $\frac{\omega_o}{2Q}\hat{k}$. This aspect is treated in the following paragraph.

2) Low Frequency Response: The low frequency dynamics between $\hat{k}(t)$ and $\hat{\omega}_{sw}(t)$ can also be modeled by the same discrete-time-domain methods described previously. In this case, the model is assumed to be a first-order low-pass filter, which after transformation in the continuous time domain yields

$$\frac{\hat{\omega}_{sw_2}(s)}{\hat{k}(s)} = \frac{\omega_o}{2Q}\frac{1}{1+\tau s+s\frac{T}{2}} \tag{16}$$

where $\hat{\omega}_{sw_2}(s)$ is the low frequency response, as shown in Fig. 11(b), and τ is a time constant that depends on the time constant of the resonant tank.

Fig. 12 shows the time-domain waveforms of j_L, m_C, and $j_L - km_C$, for two different, but constant, values of k. In the first case ($K = 0$), $j_L - Km_C$ is equal to j_L and the switching signal only depends on the sign of the inductor current , not on its amplitude. As a consequence, the settling time of j_L does not affect the switching instants and τ is equal to zero. As K increases, the dependence of the switching instants on the amplitudes of the inductor current and the capacitor voltage grows, given that sign$(j_L - Km_C)$ depends on such amplitudes. In the PRC, the inductor current and capacitor voltage settle down with a time constant $2RC$ [23]. Consequently, the settling time of ω_{sw} also approaches $2RC$ when K grows. It can be assumed that the time constant τ grows following the sinusoidal function

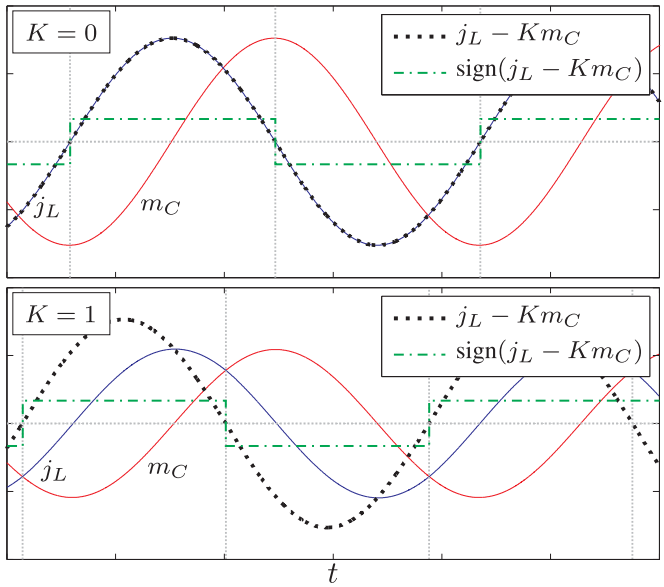

Fig. 12. Time-domain waveforms of the PRC for two different values of $K = [0, 1]$. When $K = 0$, the switching instant is only modified by the sign of j_L. When $K \neq 0$, the switching instant is affected by the time constants of j_L and m_C.

of the state variables, such that a general model can be written as follows:

$$\tau = 2RC\sin(\arctan(|K|)) = 2RC\frac{|K|}{\sqrt{1+K^2}}. \tag{17}$$

Fig. 13 shows the percentage values of τ with respect to $2RC$, for a range of values of K corresponding to angles between [0, 85] degrees. The model provides a direct way to relate the value of K and the settling time of the switching frequency. Note that

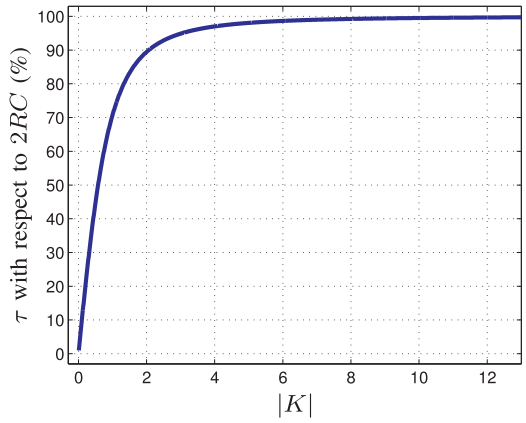

Fig. 13. Settling time τ as a function of $|K|$.

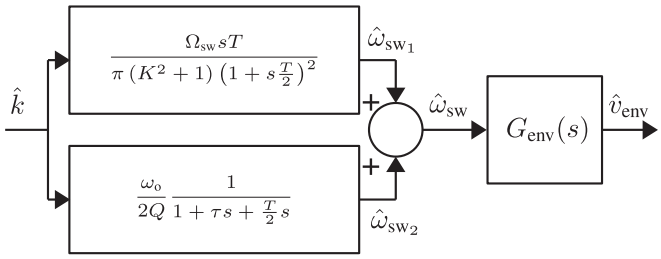

Fig. 14. Block diagram of the complete small-signal model.

the absolute value of K is used in order to avoid negative time constants when $K < 0$.

3) Complete Model: The block diagram of the complete small-signal model between the control variable $\hat{k}$ and the output $\hat{v}_{env}$ is depicted in Fig. 14. The model consists of the low and high frequency blocks with the corresponding dc gain and the frequency modulated transfer function $G_{env}(s)$, as explained in Section III-A.

In order to validate the model, Bode plots of the control-to-output transfer functions for two different loads $R = 420\,\Omega (Q = 15.2)$ and $R = 650\,\Omega (Q = 21.3)$ are shown in Fig. 15. It is worth noting that the resistances employed correspond to the nominal and worst-case loads for the proposed design example, and that the nominal load $R = 420\,\Omega$ matches the peak of the dc gain in VSS-based control, as shown previously in Fig. 10(b). The values of parameters used to plot the Bode diagram are those used before in Table I: $L = 8.3\,\mu$H, $C = 10.5\,n$F, and $V_g = 12$ V. The figure shows the analytical small-signal model (solid line) against numerical simulations of the switched circuit (circle marks) for two frequencies below resonance $f_{sw} =$ [520 kHz, 515 kHz], which match the required frequencies for an ac peak output voltage of $V_{env} = 160$ V. The values of K for these operating frequencies are enumerated in Table II. Going back to Fig. 15, it can be seen that the model is in good agreement with the simulation results and that the proposed transfer function remains valid up to frequencies below one half of the switching frequency. In addition, it is worth to remark that the VSS-based controller cancels the effects of the double pole below the switching frequency that appears

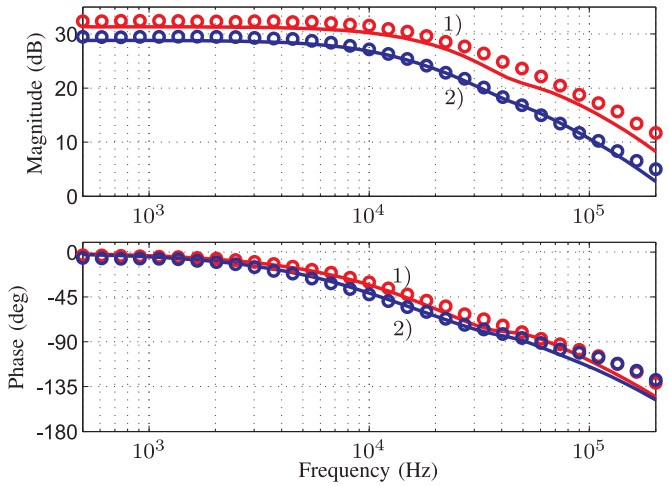

Fig. 15. Comparison between the proposed model and numerical simulations of the switched circuit for two different switching frequencies and loads: 1) 520 kHz/420 Ω . 2) 515 kHz/650 Ω . Solid-line: analytical model. O marks: numerical simulations.

TABLE II
OPERATING POINT VALUES

Q	f_{sw}	R	K	$V_{env}(V_g = 12$ V)
15.2	520 kHz	420 Ω	−2.1	160 V
21.3	515 kHz	650 Ω	−3.2	160 V

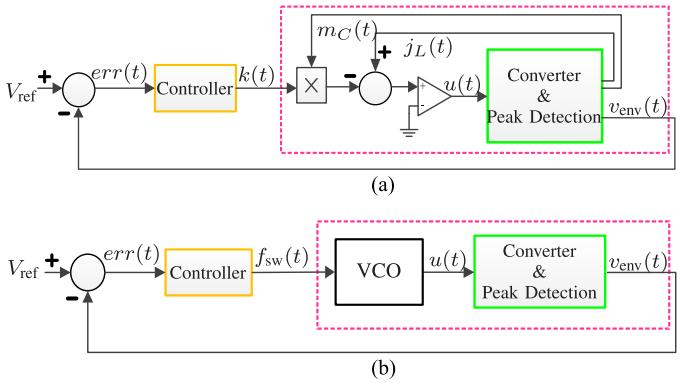

Fig. 16. Closed-loop block diagram of the resonant converter with: (a) the VSS-based controller, (b) the FM controller.

in the control-to-output transfer function with the conventional frequency modulation $G_{env}(s)$ [7]. As a consequence, with the VSS-based controller, the phase is well above 180º for the range of frequencies that can be of interest for feedback, and the system dynamics are similar to those of a first-order system, as it was also mentioned in [14]. These aspects suggest that closed-loop regulation by means of a VSS-based controller can outperform frequency modulation due to larger feedback bandwidth and improved robustness.

IV. CLOSED-LOOP VSS-BASED CONTROL

A design example showing the regulation capabilities and the benefits of the proposed technique is presented in this

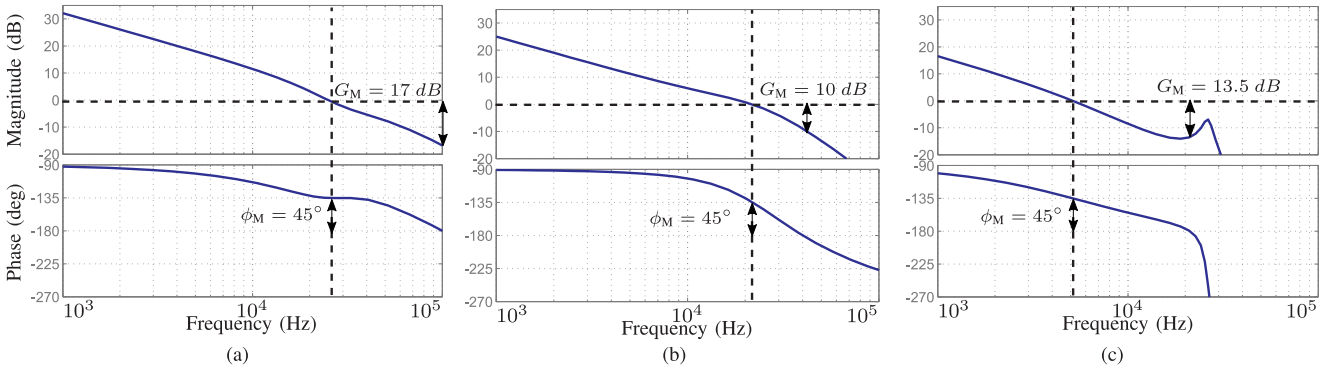

Fig. 17. Bode plot of the loop gain in: (a) proposed VSS system, (b) conventional FM control with nominal load, (c) conventional FM control with worst-case load.

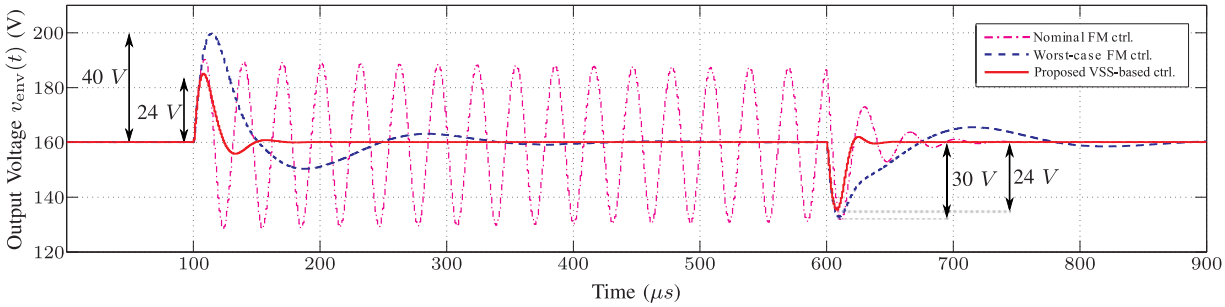

Fig. 18. Comparison between the proposed VSS-based controller and FM controller responses for a 420 Ω → 650 Ω → 420 Ω load transient with nominal input voltage. Solid-line: VSS-based controller. Dashed line: Nominal load FM controller. Dashed dotted line: Maximum load FM controller.

section. The synthesis of a controller for the regulation of the output voltage in a PRC, following the parameters and operating points given in Tables I and II, is described in three different cases. First, in the case of the proposed VSS-based control with the nominal load $R = 420\,\Omega$. Second, using standard frequency modulation (FM) in two different cases: with the nominal load of $R = 420\,\Omega$ and with the worst-case load of $R = 650\,\Omega$.

A block diagram of the converter with the controllers for the VSS and FM approaches is shown in Fig. 16. In the figure, it is worth to point out that sensing the output voltage envelope is carried out by means of a peak detector and that the FM realization requires a voltage-controlled oscillator (VCO). It is also worth to mention that the synthesized controllers follow a PI structure. They consist of an integrator for zero steady-state error, a phase leading zero for appropriate phase margin, and an additional high-frequency pole for noise immunity. In order to unify criteria for the different designs, all the controllers satisfy a phase margin ϕ_M over 45° and a gain margin G_M above 10 dB.

A. Controller Synthesis for VSS Approach

The design of the first controller, that considers the VSS approach, has been carried out by employing the model described in the previous section. Fig. 17(a) shows the loop gain of the PRC converter with the synthesized controller, considering the nominal load of $R = 420\,\Omega$

$$G_{c,\mathrm{VSS}}(s) = 3300\frac{1 + 6.9\cdot 10^{-6}s}{s(1 + 2.8\cdot 10^{-6}s)}. \tag{18}$$

As it can be seen, a phase margin of 45°together with a gain margin of 17 dB can be easily achieved with a crossover frequency f_c of approximately 25 kHz.

B. Controller Synthesis for FM and Nominal Load

The second controller is designed for the conventional FM, whose control-to-output transfer function is given by G_{env}, as mentioned previously. In this case, the nominal load $R = 420\,\Omega$ is taken into account

$$G_{c,\mathrm{FM1}}(s) = 1520\frac{1 + 8.5\cdot 10^{-6}s}{s(1 + 2.5\cdot 10^{-6}s)}. \tag{19}$$

A Bode plot of the loop gain with this controller is depicted in Fig. 17(b). A phase margin of 45° and a gain margin of exactly 10 dB are provided, for a crossover frequency of approximately 20 kHz.

C. Controller Synthesis for FM and Worst-Case Load

Finally, a third controller for FM has been designed, considering a worst-case load of $R = 650\,\Omega$. Given that, in this case, the dc gain of the control-to-output transfer function G_{env} is near its maximum value for this application [see Fig. 10(b)],

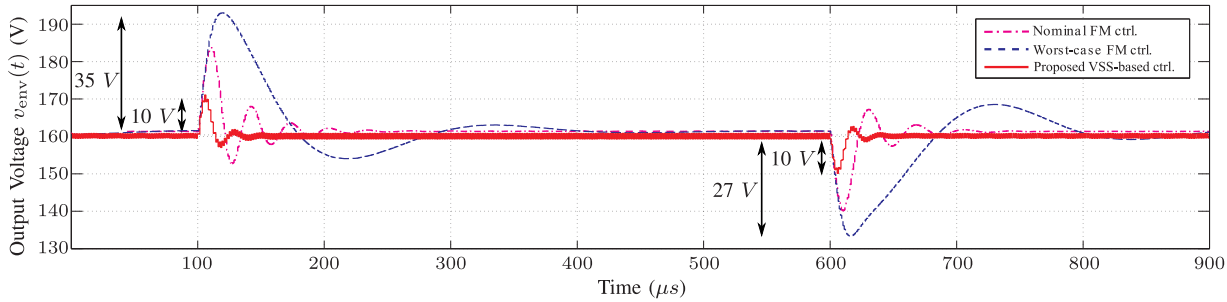

Fig. 19. Comparison between the proposed VSS and controller response for a 12 V → 14 V → 12 V input voltage transient with nominal load (420 Ω). Solid-line: VSS-based controller. Dashed line: Nominal load FM controller. Dashed dotted line: Maximum load FM controller.

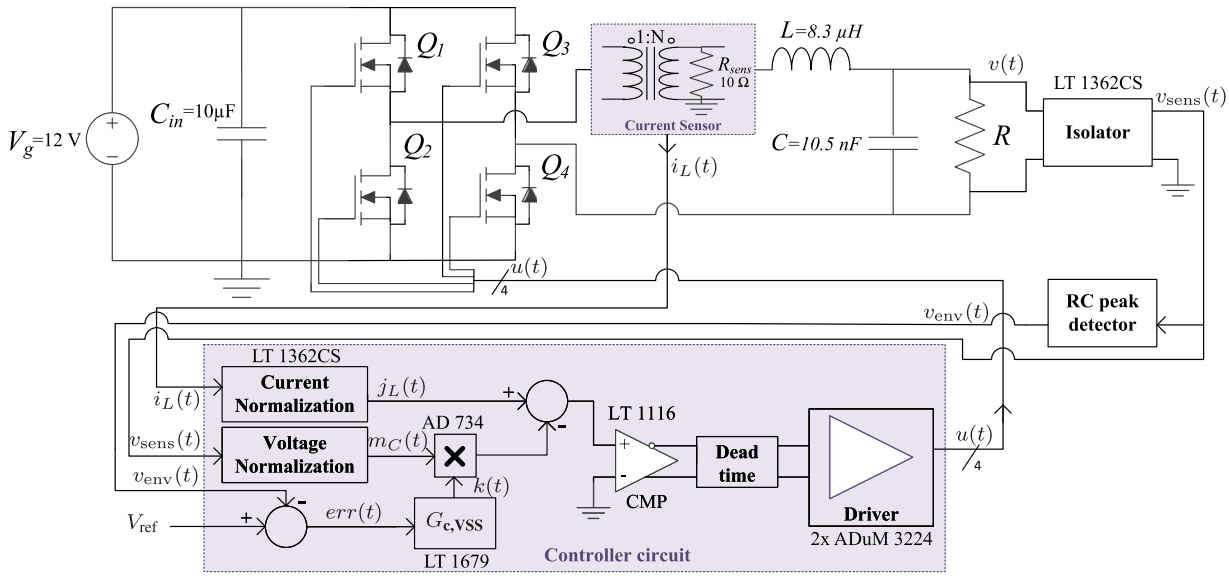

Fig. 20. Schematic of a parallel resonant converter with the proposed VSS-based controller

the crossover frequency that allows to satisfy a phase margin of 45º and a gain margin of 10 dB is lower than in the previous cases: $f_c = 5$ kHz [see Fig. 17(c)]. Besides, the use of a zero for improved phase margin provides a relatively small improvement, due to the influence of the resonant complex pole in G_{env} at high frequencies. These aspects result in a simpler and more conservative controller

$$G_{c,\text{FM2}}(s) = 426\frac{1}{s(1+3\cdot 10^{-5}s)}. \tag{20}$$

D. Simulation Results

In this section, the properties of the synthesized controllers have been illustrated with a set of simulations of the switched circuit. As in the previous section, the regulation objective is to obtain an ac peak output voltage of $V_{\text{env}} = 160$ V from an input of $V_g = 12$ V. First, the three different controllers have been tested in presence of load disturbances. Fig. 18 shows a detail of the voltage regulation waveforms when the load changes from its nominal value $R = 420\ \Omega$ to the worst case $R = 650\ \Omega$ at $t = 100\ \mu$s and goes back to $R = 420\ \Omega$ at $t = 600\ \mu$s. It can be seen that while the VSS-based controller $G_{c,\text{VSS}}(s)$ (solid line) rejects the disturbance with a voltage deviation of 24 V and a settling time below 50 μs, the FM controller $G_{c,\text{FM1}}(s)$ (dashed-line) becomes unstable and cannot regulate the output voltage

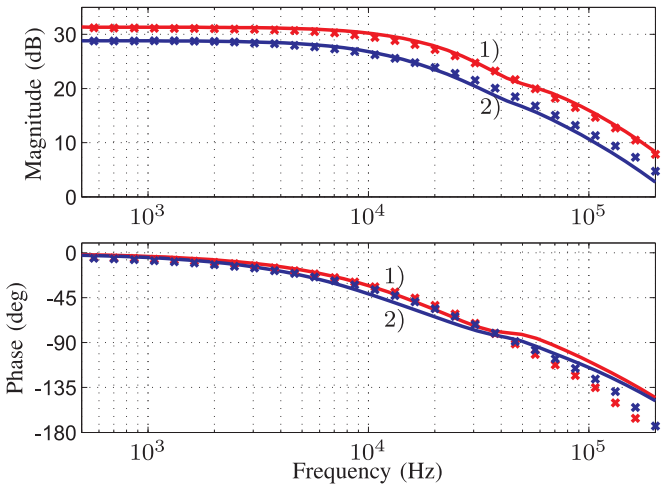

Fig. 21. Comparison between the proposed model and experimental results for two different switching frequencies and loads: 1) 520 kHz/420 Ω . 2) 515 kHz/650 Ω . Solid-line: analytical model. X marks: experimental measurements.

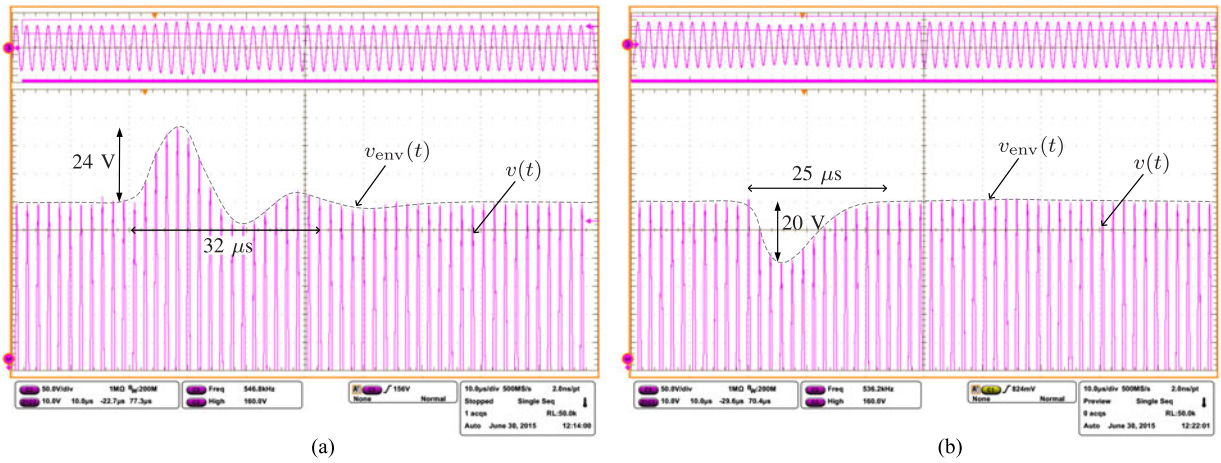

Fig. 22. Output voltage measurement under load variations ($V_g = 12$ V). (a) $R = 420\ \Omega \rightarrow 650\ \Omega$, (b) $R = 650\ \Omega \rightarrow 420\ \Omega$.

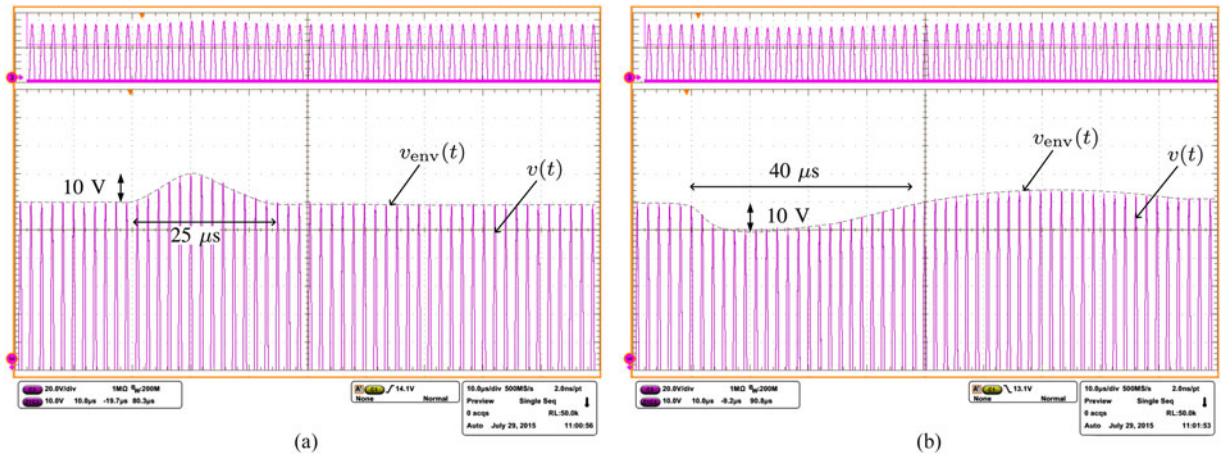

Fig. 23. Output voltage measurement under input voltage variations (R= 420 Ω). (a) $V_g = 12\ \text{V} \rightarrow 14\ \text{V}$, (b) $V_g = 14\ \text{V} \rightarrow 12\ \text{V}$.

for this range of loads. The conservative controller $G_{c,\text{FM2}}(s)$ (dash-dotted line), which has been designed using the worst-case load at $R = 650\ \Omega$, maintains the stability of the converter in both operating points, but at the expense of worse disturbance rejection properties, since the output voltage deviation and settling time are about 40 V and 250 μs, respectively.

The improved control bandwidth of the VSS-based controller $G_{c,\text{VSS}}(s)$ with respect to frequency modulation can also be regarded in case of input voltage disturbances. In Fig. 19, the input voltage V_g switches back and forth between 12 and 14 V. While the FM controllers $G_{c,\text{FM1}}(s)$ and $G_{c,\text{FM2}}(s)$ present voltage shifts above 20 and 30 V, respectively, the VSS-based controller $G_{c,\text{VSS}}(s)$ presents a deviation of the output voltage of only 10 V. Besides, the VSS-based controller yields a well-damped waveform with a settling time lower than 50 μs, in contrast with the poor damping and long settling times of the conventional controllers.

V. Experimental Results

This section presents the experimental realization of a PRC converter with the proposed VSS-based control approach and the closed-loop regulation of the output voltage envelope by means of the PI controller $G_{c,\text{VSS}}(s)$. The experimental prototype is described first. Then, the frequency response of the VSS-based controlled converter is compared with that of the proposed small-signal model. Finally, the closed-loop transients under the same load an input voltage disturbances used in the simulations are shown.

A. Experimental Setup

A 100-W experimental prototype of a PRC converter, following the specifications established in Table I, has been built. The power stage is made up of an H-bridge circuit, employing four MOSFETs (IPB200N15N3G), and a resonant tank, composed of a ceramic capacitor and an air-gap-based inductor of matching values. The VSS-based controller employs an LT1116 comparator to establish the change of polarity of the control signal and a current transformer for current sensing purposes. One of the main differences with a conventional implementation is the absence of VCO for frequency modulation. The schematic of the experimental prototype can be seen in Fig. 20. Although the PRC can operate in zero-voltage switching mode when the circuit operates above resonance ($k > 0$), operation below resonance ($k < 0$) is preferred

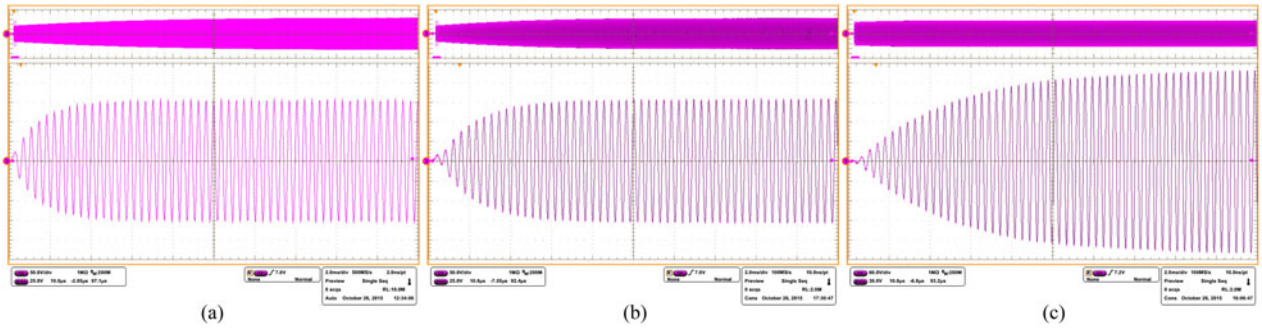

Fig. 24. Startup waveforms of the output voltage for different loads. Top: 60 V/div, 2 ms/div. Bottom: 30 V/div, 10 μs/div. (a) $R = 420\ \Omega$, (b) $R = 650\ \Omega$, (c) No load.

in the proposed example due to smaller circulating currents [24].

B. Frequency Response Verification

Two measurements of the control-to-output voltage frequency response, matching those shown in the simulations have been depicted in Fig. 21. The measurements have been carried out with a Venable FRA-3120 network analyzer and in open loop, i.e., a small ac signal $\hat{k}$ is added to the dc value of the input K and the envelope of the output voltage $\hat{v}_{\text{env}}$ is measured as the output.

Two set points have been measured, corresponding to those shown previously in Table II and Fig. 15. It can be observed a good agreement between the solid lines (analytical model) and the experimental measurements (x marks). While there exist minor discrepancies in phase responses above 50 kHz, these differences are not usually a problem for closed-loop control, given that effective bandwidths are typically lower than $\frac{1}{10}$ of the switching frequency and that phase responses are always above -180º.

C. Closed-Loop Responses

In Figs. 22 and 23, the experimental waveforms of the converter with controller $G_{c,\text{VSS}}(s)$ are shown. Again, the ac output voltage envelope is $V_{\text{env}} = 160$ V and the input voltage is $V_g = 12$ V. The ac voltage has been enlarged and its envelope outlined for easy comparison with the simulation results. It can be observed an excellent agreement between the solid lines of Figs. 18 and 19 and the waveforms in Figs. 22 and 23, which verifies the correctness of the analytical derivations and the performance of the proposed control approach.

D. Start-Up Responses

Fig. 24 shows the waveforms of the output voltage during start-up, for three different loads: 420 Ω, 650 Ω, and no load. As predicted by the proposed model, larger loads correspond to lower dc gains of the control-to-output transfer function, and consequently, to narrower control bandwidths and increased settling times. It is worth to remark that the VSS-based controller allows the soft-start of the circuit without any need of additional devices or control laws, which helps the designer to obtain a cost-effective circuit.

VI. Conclusion

Self-oscillating resonant converters under VSS-based control laws can provide improved closed-loop performances, due to the inherent half-period sampling and its simpler dynamics, besides of other advantages in their realization, as for example, the lack of voltage-controlled oscillator. This paper presents a novel small-signal model for these self-oscillating resonant converters under a class of VSS-based control laws and explains the benefits obtained with the resulting VSS-based controller. The proposed modeling approach exploits the link between the control variable k, the angle between the input current and the input voltage, and the switching frequency, yielding an expression that can be well represented by a linear approximation. This linear approximation is employed together with an analysis of the trajectories of the system in the state plane in order to derive the small-signal control-to-switching frequency transfer functions. The proposed approach has the advantage that the model can be coupled with the well-known switching frequency-to-output transfer function for frequency modulation so that a complete control-to-output voltage transfer function can be obtained easily. Although the model is the result of a linearization around $K = 0$, it has been shown that its range of validity is sufficient to regulate the converter over a wide range of frequencies.

This model is used as the basis for designing a VSS-based controller able to regulate the output voltage envelope of a parallel resonant converter under variations of the input and output parameters. The synthesized controller, which has been designed for the nominal load, has been compared with a conventional controller for frequency modulation, in nominal and worst-case conditions. Simulations have shown that the VSS-based controller outperforms frequency modulation by providing not only tight regulation in the presence of disturbances, but also exhibiting robustness in case of significant parametric uncertainty.

Finally, the experimental realization of a self-oscillating PRC converter with the proposed VSS-based controller has demonstrated the correctness of the proposed small-signal model and the validity of the closed-loop simulation results. Further research contemplates the extension of the proposed modeling technique to other resonant converters, such as the series resonant converter. Potential applications of this research includes efficient lighting systems [25], [26] or induction heating [27], where the proposed control technique can be used as a simple and robust mechanism for regulating circuits with large sets of uncertainty.

REFERENCES

[1] W. Feng, F. C. Lee, and P. Mattavelli, "Optimal trajectory control of LLC resonant converters for LED PWM dimming," *IEEE Trans. Power Electron.*, vol. 29, no. 2, pp. 979–987, Feb. 2014.

[2] R. Schnell, R. Zane, and F. Azcondo, "Size reduction in low-frequency square-wave ballasts for high-intensity discharge lamps using soft-saturation magnetic material and digital control techniques," *IEEE Trans. Power Electron.*, vol. 28, no. 2, pp. 1036–1046, Feb. 2013.

[3] P. Teodosescu, M. Bojan, and R. Marschalko, "Resonant led driver with inherent constant current and power factor correction," *Electron. Lett.*, vol. 50, no. 15, pp. 1086–1088, Jul. 2014.

[4] O. Lucia, J. M. Burdio, I. Millan, J. Acero, and D. Puyal, "Load-adaptive control algorithm of half-bridge series resonant inverter for domestic induction heating," *IEEE Trans. Ind. Electron.*, vol. 56, no. 8, pp. 3106–3116, Aug. 2009.

[5] H. Sarnago, O. Lucia, A. Mediano, and J. Burdio, "High-efficiency parallel quasi-resonant current source inverter featuring sic metal-oxide semiconductor field-effect transistors for induction heating systems with coupled inductors," *IET Power Electron.*, vol. 6, no. 1, pp. 183–191, Jan. 2013.

[6] Y. Yin, R. Zane, J. Glaser, and R. W. Erickson, "Small-signal analysis of frequency-controlled electronic ballasts," *IEEE Trans. Circuits Syst. I, Fundam. Theory Appl.*, vol. 50, no. 8, pp. 1103–1110, Aug. 2003.

[7] Y. Yin, R. Zane, R. W. Erickson, and J. Glaser, "Direct modeling of envelope dynamics in resonant inverters," in *Proc. IEEE Power Electron. Spec. Conf.*, Jun. 15–19, 2003, vol. 3, pp. 1313–1318.

[8] C. Brañas, F. J. Azcondo, and R. Zane, "Power-mode control of multiphase resonant electronic ballast," *IEEE Trans. Ind. Electron.*, vol. 59, no. 4, pp. 1770–1778, Apr. 2012.

[9] V. Vorperian, "Approximate small-signal analysis of the series and the parallel resonant converters," *IEEE Trans. Power Electron.*, vol. 4, no. 1, pp. 15–24, Jan. 1989.

[10] C. T. Rim and G. H. Cho, "Phasor transformation and its application to the DC/AC analyses of frequency phase-controlled series resonant converters (SRC)," *IEEE Trans. Power Electron.*, vol. 5, no. 2, pp. 201–211, Apr. 1990.

[11] S. Glozman and S. Ben-Yaakov, "Dynamic interaction analysis of HF ballasts and fluorescent lamps based on envelope simulation," *IEEE Trans. Ind. Appl.*, vol. 37, no. 5, pp. 1531–1536, Sep./Oct 2001.

[12] R. Oruganti and F. C. Lee, "Resonant power processors, part I—State plane analysis," *IEEE Trans. Ind. Appl.*, vol. IA-21, no. 6, pp. 1453–1460, Nov. 1985.

[13] R. Oruganti and F. C. Lee, "Resonant power processors, part II—Methods of control," *IEEE Trans. Ind. Appl.*, vol. IA-21, no. 6, pp. 1461–1471, Nov. 1985.

[14] M. G. Kim, D. S. Lee, and M. J. Youn, "A new state feedback control of resonant converters," *IEEE Trans. Ind. Electron.*, vol. 38, no. 3, pp. 173–179, Jun. 1991.

[15] L. Rossetto, "A simple control technique for series resonant converters," *IEEE Trans. Power Electron.*, vol. 11, no. 4, pp. 554–560, Jul. 1996.

[16] H. Sira-Ramirez and R. Silva-Ortigoza, "On the control of the resonant converter: A hybrid-flatness approach," presented at the 15th Int. Symp. Mathematical Theory Networks Systems, Notre Dame, IN, USA, 2002.

[17] A. J. Gilbert, C. M. Bingham, D. A. Stone, and M. P. Foster, "Self-oscillating control methods for the LCC current-output resonant converter," *IEEE Trans. Power Electron.*, vol. 23, no. 4, pp. 1973–1986, Jul. 2008.

[18] D. Williams, C. Bingham, M. Foster, and D. Stone, "Hamel locus design of self-oscillating DC-DC resonant converters," *IET Power Electron.*, vol. 3, no. 1, pp. 86–94, 2010.

[19] M. Momeni, H. M. Kelk, and H. Talebi, "Rotating switching surface control of series-resonant converter based on a piecewise affine model," *IEEE Trans. Power Electron.*, vol. 30, no. 3, pp. 1762–1772, Mar. 2015.

[20] H. Molla-Ahmadian, F. Tahami, A. Karimpour, and N. Pariz, "Hybrid control of DC-DC series resonant converters: The direct piecewise affine approach," *IEEE Trans. Power Electron.*, vol. 30, no. 3, pp. 1714–1723, Mar. 2015.

[21] V. Utkin, "Variable structure systems with sliding modes," *IEEE Trans. Autom. Control*, vol. AC-22, no. 2, pp. 212–222, Apr. 1977.

[22] R. Bonache-Samaniego, C. Olalla, and L. Martinez-Salamero, "Design of self-oscillating resonant converters based on a variable structure systems approach," *IET Power Electron.*, vol. 9, pp. 111–119, 2015, doi: http://dx.doi.org/10.1049/iet-pel.2014.0964.

[23] R. V. Langmuir, "Repetitively switched circuits," *IEEE Trans. Aerosp. Electron. Syst.*, vol. AES-9, no. 1, pp. 59–64, Jan. 1973.

[24] R. W. Erickson and D. Maksimovic, *Fundamentals of Power Electronics*. New York, NY, USA: Springer, 2001.

[25] M. Kadota, H. Shoji, and S. Furuya, "A dimming method for hot cathode fluorescent lamp using a resonant inverter operating at fixed switching frequency," *IEEE Trans. Power Electron.*, vol. 30, no. 4, pp. 2253–2261, Apr. 2015.

[26] X. Wu, C. Hu, J. Zhang, and Z. Qian, "Analysis and design considerations of LLCC resonant multioutput DC/DC led driver with charge balancing and exchanging of secondary series resonant capacitors," *IEEE Trans. Power Electron.*, vol. 30, no. 2, pp. 780–789, Feb. 2015.

[27] O. Jimenez, O. Lucia, I. Urriza, L. Barragan, and D. Navarro, "Power measurement for resonant power converters applied to induction heating applications," *IEEE Trans. Power Electron.*, vol. 29, no. 12, pp. 6779–6788, Dec. 2014.

Ricardo Bonache-Samaniego received the B.S. and the M.S. degrees in industrial electronics engineering from Universitat Rovira i Virgili, Tarragona, Spain, in 2009 and 2011, respectively, where he is currently working toward the Ph.D. degree.

He worked as an Engineer in the field of autonomous robotics with the company m-BOT Solutions S.L in the period 2010–2011. Since 2011, he has been a member of the Automatic Control and Industrial Electronics Research Group, Universitat Rovira i Virgili. He worked as a Lecture Assistant in the period 2015–2016 and he was a Visiting Scholar in 2016 at Colorado Power Electronics Center, University of Colorado, Boulder, CO, USA for four months. His research interests include the modeling and control of switching power converters with particular emphasis on high-efficiency resonant converters, self-oscillating resonant converters, and novel topologies for battery management, charge of electric vehicles and lightning systems.

Carlos Olalla (S'06–M'09) received the M.S. degree in industrial electronics engineering from Universitat Rovira i Virgili, Tarragona, Spain, in 2004, and the Ph.D. degree in advanced automatic control from Universitat Politècnica de Catalunya, Barcelona, Spain, in 2009.

In 2007 and 2009, he was a visiting scholar at the *Laboratoire d'Analyse et d'Architecture des Systèmes* (LAAS-CNRS), Toulouse, France, where he also held a postdoctoral position until March 2010. From 2010 to 2012 he was a visiting scholar and a research associate in the Colorado Power Electronics Center (CoPEC), University of Colorado, Boulder, USA. Since 2013, he has been a Beatriu de Pinós and a Marie Curie research fellow with the Dept. of Electrical, Electronics and Automatic Control Engineering, Universitat Rovira i Virgili. His research interests include the modeling, optimization and robust control of power converters and renewable energy systems.

Luis Martínez-Salamero (M'85–SM'12) received the Ingeniero de Telecomunicación and the Doctorate degrees from the Universidad Politécnica de Cataluña, Barcelona, Spain, in 1978 and 1984, respectively.

From 1978 to 1992, he taught circuit theory, analog electronics, and power processing at Escuela Técnica Superior de Ingenieros de Telecomunicación de Barcelona, Barcelona. During the academic year 1992–1993, he was a Visiting Professor at the Center for Solid State Power Conditioning and Control, Department of Electrical Engineering, Duke University, Durham, NC, USA. He is currently a Full Professor at Universidad Rovira i Virgili, Tarragona, Spain. During the academic years 2003–2004 and 2010–2011, he was a Visiting Scholar at Laboratoire d'Architecture et d'Analyse des Sytèmes of the National Centre for Scientific Research, Toulouse, France.

Dr. Martinez-Salamero was a Distinguished Lecturer of the IEEE Circuits and Systems Society from 2001 to 2002 and the President of the IEEE Spanish Joint Chapter of the IEEE Power Electronics and Industrial Electronics Societies from 2005 to 2008.